ADVANCED ELECTRONIC MATERIALS Open Access
www.advelectronicmat.de

Mobility-Lifetime Products in Organic Infrared Photodiodes with Peak Absorption at 1550 nm

*Bogyeom Seo, Tyler Bills, Paramasivam Mahalingavelar, Woojo Kim, Hyeong Ju Eun, Jong H. Kim, Jason D. Azoulay, and Tse Nga Ng**

Infrared photodiodes based on organic semiconductors are promising for low-cost sensors that operate at room temperature. However, their realization remains hampered by poor device efficiency. Here, performance limitations are analyzed by evaluating the mobility-lifetime products and charge collection efficiency of devices operating in the shortwave infrared with a peak absorption at 1550 nm. Through complementary impedance and current-voltage measurements on devices with different donor-to-acceptor semiconductor ratios, a trade-off between mobility and recombination time and the need to balance between transport and interfacial charge transfer are observed. Thus, this study revisits the mobility-lifetime metric to shed new light on charge collection constraints in organic infrared photodiodes.

1. Introduction

Recent advances in narrow bandgap conjugated polymers have demonstrated the potential of these semiconductor materials for infrared sensing technologies that benefit from low-cost fabrication and room-temperature operation.[1–11] However, organic infrared photodetectors are far less developed than those operating in the visible region of the electromagnetic spectrum, with new challenges arising from numerous additional design constraints such as a higher probability of charge recombination[12] as the semiconductor bandgap decreases. Non-radiative recombination processes[13,14] hinder the collection of photogenerated charge, reducing the photocurrent. Meanwhile, generation-recombination events in the dark increase the device noise,[15,16] further diminishing the signal-to-noise ratio and overall detectivity, D^*, the figure of merit for detector sensitivity.

To improve the detectivity of organic infrared photodetectors, this work evaluates recombination losses and the efficiency of charge collection in a set of diodes operating in the shortwave infrared at 1550 nm. In these devices, charge collection efficiency was related to the carrier drift length based on the Hecht equation.[17,18] The drift length L_{drift} is defined as $L_{drift} = \mu\tau E$, where μ is the charge carrier mobility, τ is the charge lifetime, and E is the electric field. A larger mobility-lifetime product $\mu\tau$ indicates a longer travel distance at a given field, signifying lower recombination losses to facilitate charge extraction at the electrodes.

The mobility-lifetime product has been studied extensively in organic solar cells,[19–22] but studies related to infrared polymers remain nascent. In this study, the composition of the photosensitive layer was adjusted to determine the effect of varying donor-to-acceptor ratios on $\mu\tau$ and to establish correlations with device noise, external quantum efficiency (EQE), and detectivity. In addition, the impact of the semiconductor blend ratio on the density of states (DOS) in the active layer was examined using impedance measurements[23–27] to compare profiles of sub-bandgap states, which may act as recombination centers and consequently affect $\mu\tau$ and charge collection. The photodiode with the highest $\mu\tau$ was characterized in terms of response speed and dynamic range. This study shows the utility of revisiting the $\mu\tau$ metric to better understand charge collection limits in novel organic infrared photodiodes.

2. Results and Discussion

2.1. Device Characteristics: Noise, External Quantum Efficiency, Detectivity

Figure 1a presents the chemical structures of the infrared conjugated polymers used in this study. The donor polymer was

B. Seo, W. Kim, T. N. Ng
Department of Electrical and Computer Engineering
University of California San Diego
9500 Gilman Drive, La Jolla, CA 92093-0407, USA
E-mail: tnn046@ucsd.edu
T. Bills, P. Mahalingavelar, J. D. Azoulay
School of Chemistry and Biochemistry and School of Materials Science and Engineering
Georgia Institute of Technology
Atlanta, GA 30332, USA
H. J. Eun, J. H. Kim
Department of Molecular Science and Technology
Ajou University
Suwon 16499, Republic of Korea

The ORCID identification number(s) for the author(s) of this article can be found under https://doi.org/10.1002/aelm.202400816

DOI: 10.1002/aelm.202400816

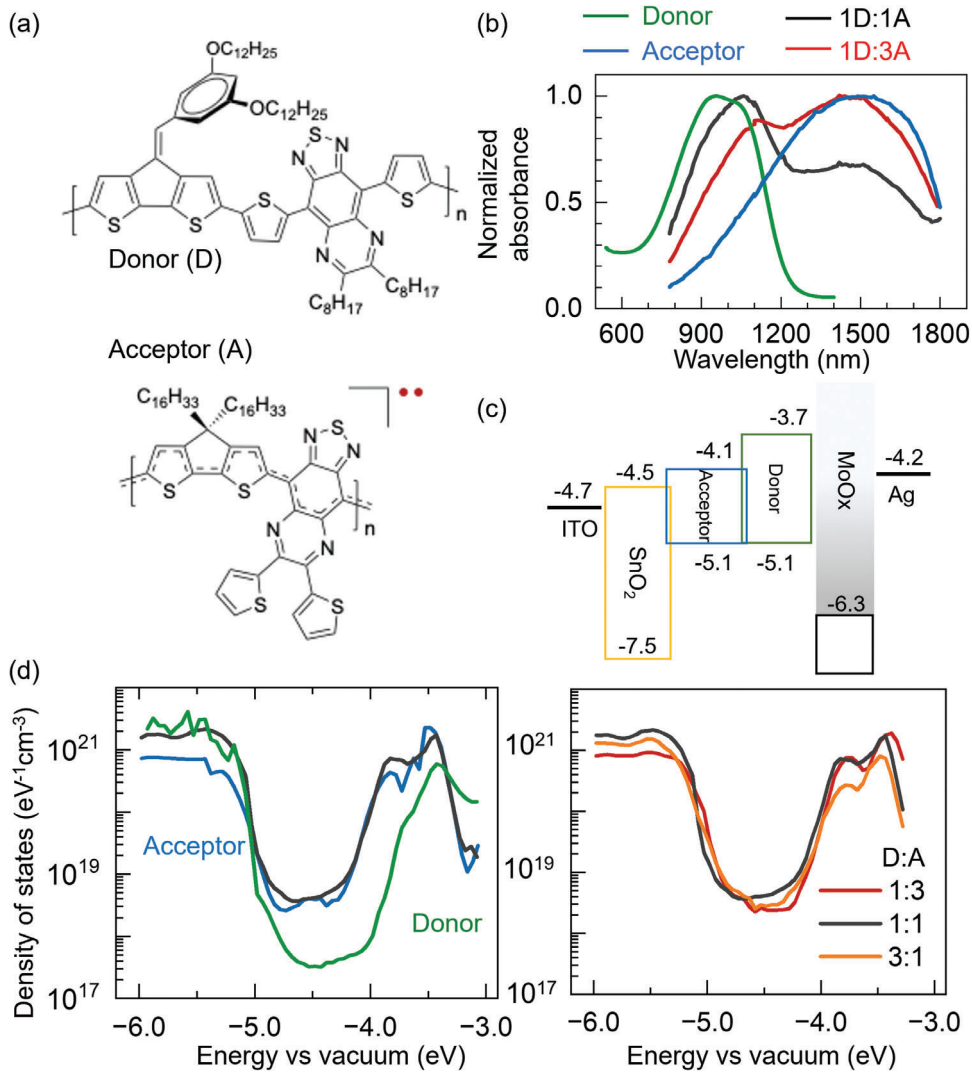

Figure 1. a) Chemical structures of the polymeric semiconductors. b) Normalized absorption spectra of neat and blend films. c) Energy band diagram of the materials in the photodiode structure. d) DOS versus energy level for the neat films and bulk heterojunction blends. The 1D:1A blend was denoted by the black curve and included in both plots for a comparison between neat versus blend films.

poly(4-(5-(4-(3,5-bis-(dodecyloxy)benzylidene)-4*H*-cyclopenta-[2,1-*b*:3,4-*b*']-dithiophen-2-yl)thiophen-2-yl)-6,7-dioctyl-9-(thiophen-2-yl)-[1,2,5]thiadiazolo[3,4-*g*]quinoxaline), which has an absorption maximum (λ_{max}) at 1100 nm.[1,28] The acceptor polymer, poly(4-(4,4-dihexadecyl-4*H*-cyclopenta[2,1-*b*:3,4-*b*']dithiophen-2-yl)-6,7-di(thiophen-2-yl)-[1,2,5]thiadiazolo[3,4-*g*]quinoxaline) has a λ_{max} = 1550 nm.[29] The donor and acceptor polymers were blended at 3:1, 1:1, and 1:3 ratios by weight to form bulk heterojunction (BHJ) films. In Figure 1b and Figure S1 (Supporting Information), the normalized absorbance of BHJ films indicates that the peak absorption of the 1:1 blend was 1100 nm on account of the stronger absorption of the donor. In the1:3 blends, the maximum absorption shifts to 1550 nm consistent with the acceptor polymer forming the bulk of the films. Therefore, our study focused on devices with more acceptor contribution to increase the photoresponse at 1550 nm. All devices were fabricated using an ITO/SnO_2/donor:acceptor/MoOx/Ag architecture as shown in Figure 1c with the only variable being the photoactive layer, which either had different BHJ ratios or was a neat acceptor film.

Individual photoactive films were measured using energy-resolved electrochemical impedance spectroscopy (ER-EIS)[30,31] for comparison of the density-of-state (DOS) distributions intrinsic to the semiconductors prior to device integration. DOS is the number of available states per unit volume that charge carriers can occupy at each energy level. By sweeping the applied voltage in ER-EIS (detailed procedure presented in Figure S2, Supporting Information), the sample DOS is mapped across the energy spectrum from the highest occupied molecular orbital (HOMO) to the lowest unoccupied molecular orbital (LUMO). Structural disorder and defects[30,32–34] in the organic films may broaden the DOS at the band edges or create localized trap states in the band gap affecting charge recombination and transport.

Figure 1d compares the DOS of neat films (donor: green curve; acceptor: blue curve), where the HOMO level was the same for both films at −5.1 eV. The LUMO level was measured to be −4.1

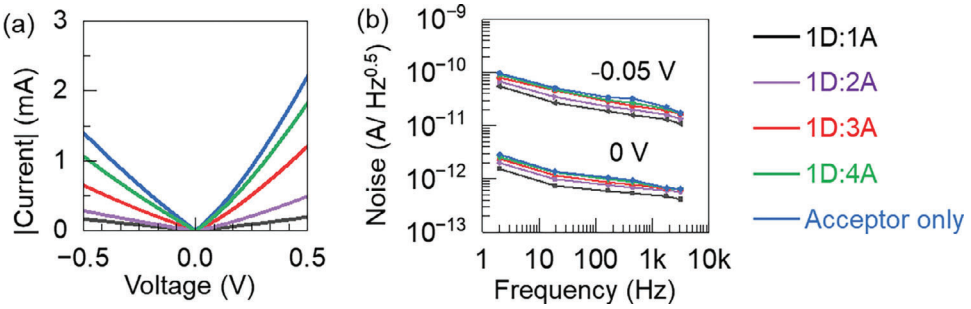

Figure 2. a) Current versus voltage characteristic and b) measured noise current versus frequency of photodiodes in the dark at different applied voltages.

eV for the acceptor and -3.7 eV for the donor. The donor film showed a DOS of $\approx 10^{17}$ eV^{-1} cm^{-3} in the bandgap, which was tenfold lower than the acceptor with a DOS of $\approx 10^{18}$ eV^{-1} cm^{-3}. As the donor and acceptor were mixed to form a BHJ, the DOS profile mostly followed the acceptor on account of its narrower bandgap than the donor. The total DOS of the blends matched or slightly exceeded the sum of individual neat films at each energy level. Considering the measurement uncertainties in Figure 1d, it was difficult to differentiate the DOS of films with various blend ratios using ER-EIS. However, after the films were integrated into photodiodes, device current and impedance measurements allowed for analysis of the relationship between blend ratios, subbandgap DOS, and device performance, as discussed below.

Figure 2 presents the dark current and noise spectral density of devices with donor:acceptor ratios of 1:1, 1:2, 1:3, and 1:4, and solely acceptor comprising the photoactive layers. The dark current primarily reflected shot noise and leakage contributions under applied biases, whereas the noise spectral density accounted for all noise components (shot, thermal, 1/f, etc.). Figure S3 (Supporting Information) shows the dark current as a function of electric field, which accounted for the thickness differences of active layers, and it shows the same trend as Figure 2. Figure S3 (Supporting Information) shows the device structure used in this paper, and it demonstrated good rectification when used with wider bandgap materials. However, when we used this same structure with our infrared acceptor which had a bandgap of 0.8 eV, the rectification decreased significantly. The dark current and noise spectral density increased with higher acceptor content because the narrower bandgap of the acceptor led to more generation-recombination events, as thermalization could more easily overcome a smaller energy difference between band states. This trend indicated the caveat of using a simple acceptor-only film, where noise levels were higher compared to that of blended semiconductors and could potentially be suppressed with an insulator blend.[1]

Figure 3a provides examples of the photodiodes' temporal response under light modulation with a 1550 nm laser, enabling comparisons of signal-to-noise characteristics as a function of the photoactive layer. As the acceptor content increased, the dark current I_{dark} rose in the order of 1:1 BHJ < 1:2 BHJ < 1:3 BHJ < 1:4 BHJ < acceptor-only device, with the neat acceptor exhibiting the worst noise. On the other hand, the photocurrent increased when using a higher proportion of acceptor. The photocurrent is defined as $I_{ph} = I_{illumination} - I_{dark}$, where $I_{illumination}$ is the apparent current under illumination. For instance, in Figure 3a, the photocurrent was 20 nA for the 1:1 BHJ and nearly tripled to 60 nA for the photodiodes with 1:3 BHJ or neat acceptor. The difference in photodiode response under light modulation was captured as a function of applied bias to calculate the EQE in Figure 3b, according to the equation $EQE = (I_{ph}/P)(hc/q\lambda)$, where P is the incident light power, h is the Planck's constant, c is the speed of light, q is electron charge, and λ is the incident light wavelength. The acceptor-only device initially displayed a similar EQE to the 1:3 BHJ at low voltage; but above -0.1 V, the 1:3 BHJ showed the highest EQE of 0.1%, followed by the 1:4 BHJ, the neat acceptor, the 1:2 BHJ and then the 1:1 BHJ.

As shown in Figure 3c, the detectivity D^* was calculated from the EQE and noise measurements by $D^* = EQE(q\lambda/hc)(A\Delta f)^{0.5}/I_{noise}$, where A is the device area, Δf is the detection bandwidth, I_{noise} is the spectral noise measured in the dark. For Figure 3c the I_{noise} was measured using a lock-in amplifier set at $\Delta f = 1$ Hz. The detectivity was high at 0 V due to minimal noise without an applied bias. A drop in detectivity was observed at low bias due to increasing background noise; however, the increase in signal began outpacing the increase in noise at higher voltages to deliver a gradual rise in detectivity. Although the photodiode with the acceptor-only active layer exhibited larger EQEs compared to the 1:1 BHJ, its detectivities were lower because of higher noise. The detectivity increased in the following order: neat acceptor < 1:4 BHJ < 1:1 BHJ < 1:2 BHJ < 1:3 BHJ, with the 1:3 BHJ achieving a detectivity of 3.7×10^7 $cmHz^{0.5}/W$ under 1550 nm light. In the analysis below, we showed data at a low bias of −0.05 V where detectivity was at its lower bound, while data at a higher bias of −0.5 V was also presented for a more typical performance under bias. The performance differences among the devices are further analyzed by evaluating the mobility-lifetime product and trap density in the next section. The 1:3 ratio showed the best balance between mobility and lifetime, which directly reflects the device's performance in terms of drift length in **Table 1**.

2.2. Comparison of Mobility-Lifetime Products and Charge Collection Efficiency

Here, the mobility-lifetime product $\mu\tau$ was determined by complementary measurements of impedance and current-voltage characteristics, and subsequently compared to model fitting results based on the Hecht equation. In **Figure 4a**, as a small sine wave perturbation was applied to the photodiode across the

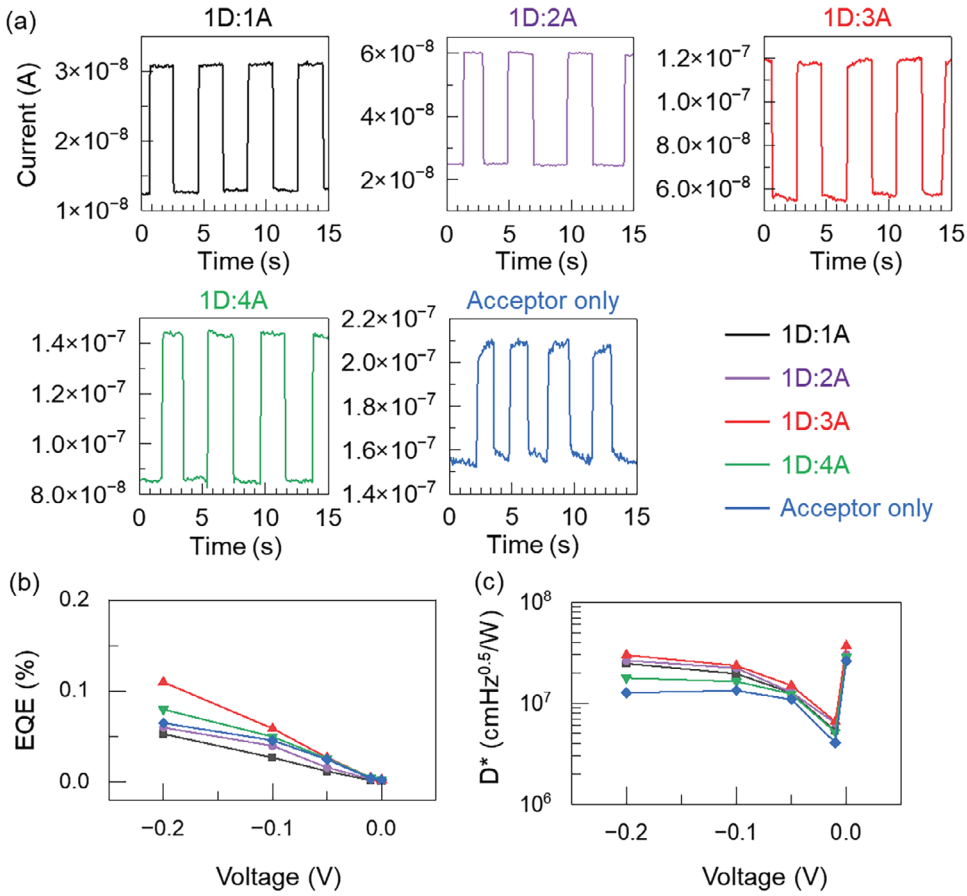

Figure 3. a) Photocurrent versus time of photodiodes at 0 V bias. b) EQE and c) detectivity versus applied bias. All measurements were taken under 18 mW cm^{-2} illumination from a 1550 nm laser diode. The color legends in part (a) also apply to (b) and (c).

frequency range, the peak in the imaginary impedance indicated the frequency at which carrier recombination was at its maximum. The recombination frequency f was converted to carrier lifetime using $\tau = (2\pi f)^{-1}$ and the resulting values are listed in Table 1. The recombination frequency as a function of applied bias is included in Figure S5 (Supporting Information).

The acceptor-only device showed the shortest lifetime before recombination. This finding was corroborated by the DOS extracted from capacitance-frequency measurements,[25–27] where the small sine wave perturbation probed and revealed the sub-bandgap DOS in Figure 4b (calculations detailed in Experimental Section). Since sub-bandgap states often acted as charge trapping and recombination sites, the large sub-bandgap DOS in the acceptor-only device was not favorable for extending carrier lifetime. In contrast, lower levels of sub-bandgap DOS were observed in the 1:3 and 1:1 BHJ, consistent with their longer lifetimes. The sub-bandgap DOS was in the sequence of acceptor-only > 1:4> 1:3> 1:2 > 1:1 BHJ, resulting in a lifetime in the order of 1:1 > 1:2 > 1:3 > 1:4 > acceptor-only.

Alongside carrier lifetime, carrier mobility is an equally important factor for determining charge collection efficiency, leading to the mobility-lifetime product as an essential parameter for analysis. The mobility μ was estimated from current-voltage characteristics using measurements of the space-charge limited current:[35] $J = (9/8)\ \varepsilon_0\ \varepsilon_r\ \mu\ \exp(\gamma\ E^{0.5})V^2/d^3$, where J is the current density, ε_0 is the vacuum permittivity, ε_r is the relative

Table 1. Measured parameters of photodiodes.

Donor: acceptor ratio	Dark noise at 0 V at 2 Hz [pA/$Hz^{0.5}$]	Dark noise at −0.05 V at 2 Hz [pA/$Hz^{0.5}$]	Carrier lifetime at −0.5V [μs]	Mobility [10^{-5} cm^2/Vs]	Mobility*lifetime [10^{-11} cm^2/V]	L_{drift} at E = −0.5 V per 200 nm [nm]
1:1	1.6	55	3	3	9	23
1:2	1.9	65	2.5	4.8	12	30
1:3	2.4	81	2	9	18	45
1:4	2.8	91	1.1	15	16.5	42
Acceptor only	3.0	97	0.8	20	16	40

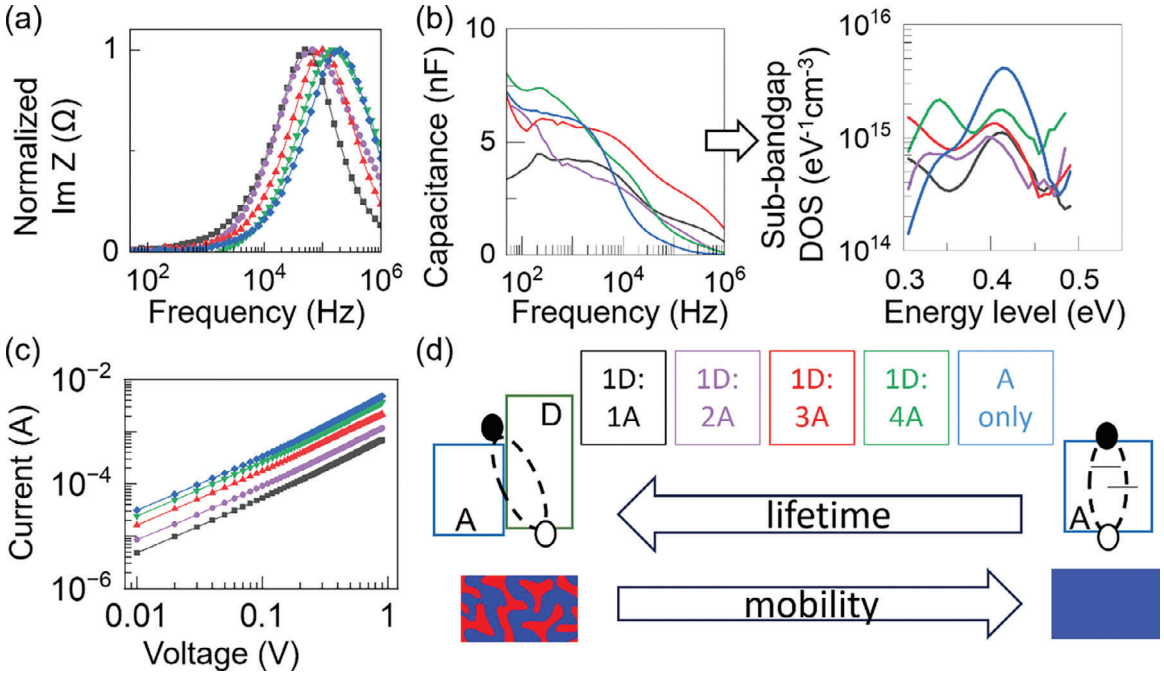

Figure 4. a) Normalized imaginary impedance versus frequency at -0.5 V bias. b) Capacitance versus frequency at -0.05 V bias (left), used to extract the DOS versus energy level away from the band edge (right). c) Current-voltage characteristics. All measurements were performed in the dark. d) Illustration of trends in recombination lifetime and mobility.

permittivity (typically assumed to be ≈3 for semiconducting polymers), γ is the electric-field coefficient[35] to the mobility (assumed to be 0.01 $cm^{0.5}/V^{0.5}$), V is the applied bias and d is the device thickness. The fit values extracted from the data in Figure 4c are presented in Table 1, and the mobility was on the order of 10^{-5} to 10^{-4} cm^2 Vs^{-1}, with the mobility of the acceptor-only device > 1:4 > 1:3 > 1:2 > 1:1 BHJ. This mobility trend was consistent with reduced disorder in the neat acceptor film, which had less interfacial disorder and more direct pathways for charge transport compared to the BHJs with tortuous percolation between donor and acceptor domains. It may seem contradictory to the finding in Figure 4b where the acceptor-only device had more deep traps. However, this mobility trend can be explained by considering that deep traps primarily affected recombination lifetime (by Shockley-Read-Hall mechanism) rather than charge transport, which occurred close to the band edge and was more impacted by shallow traps induced by disorder.

As a function of donor:acceptor ratios, the $\mu\tau$ product was the highest for the device with a 1:3 BHJ, corresponding with the EQE results. The opposing trends of carrier lifetime and mobility depicted in Figure 4d demonstrate that lifetime increased with extended delocalization across donor-acceptor interfaces, while mobility decreased with more interfaces. As such, the 1:3 BHJ balanced the competing requirements to perform better than other compositions. The mobility-lifetime metric ($\mu\tau$) includes the effects of morphology and phase separation, capturing how they influence transport and recombination. To keep the analysis focused, we fixed the interfacial layers to minimize other variables and highlight the role of charge collection in the device's performance. Given the $\mu\tau$ products in Table 1, at an electric field of −0.5 V per 200 nm, the calculated carrier drift length ($L_{drift} = \mu\tau E$) of the 1:3 BHJ would be 45 nm. This is roughly five times smaller than the ≈200 nm film thickness, implying low charge collection efficiency based on the Hecht equation:[14,17,18]

$$\frac{Q}{Q_0} = \frac{\mu\tau E}{d}\left(1 - \exp\left(-\frac{d}{\mu\tau E}\right)\right) = \frac{L_{drift}}{d}\left(1 - \exp\left(-\frac{d}{L_{drift}}\right)\right) \quad (1)$$

where Q/Q_0 is the fraction of photogenerated charge collected by the electrodes and not lost to recombination, d is the active layer thickness, and $E = (V - V_{oc})/d$ is the applied electric field accounting for the built-in open circuit voltage V_{oc}.

The 1:3 ratio showed the best balance between mobility and lifetime in terms of the drift length parameter in Table 1. In Table 1, the drift lengths were in the order of 1:3 > 1:4 > A-only > 1:2 > 1:1, and this trend reflects the EQE results in Figure 2b. This trend suggests that the acceptor material contributed to the 1550 nm absorption, while the donor material played a role in lowering the sub-bandgap DOS, which enhanced carrier lifetime.

As the photodiode with 1:3 BHJ showed the best performance, it was characterized further in **Figure 5**. In Figure 5a the normalized photocurrent of the device with the 1:3 BHJ was fitted to Equation 1, and the $\mu\tau$ fit value was found to be in the range of ≈1.5×10^{-10} cm^2 V^{-1}. This fitting and the estimation methods in Table 1 were complementary and validated each other. This value is an order of magnitude lower than organic photodiodes operating in the visible spectrum.[14,17–20] The charge collection efficiency $\eta_{collect} = Q/Q_0$ was calculated as a function of $\mu\tau$ to demonstrate the impact of improving $\mu\tau$ on the charge collection efficiency, which could reach 65% at -1 V if $\mu\tau$ is tripled to 4.5×10^{-10} cm^2 V^{-1}. Thus, there is room to enhance the

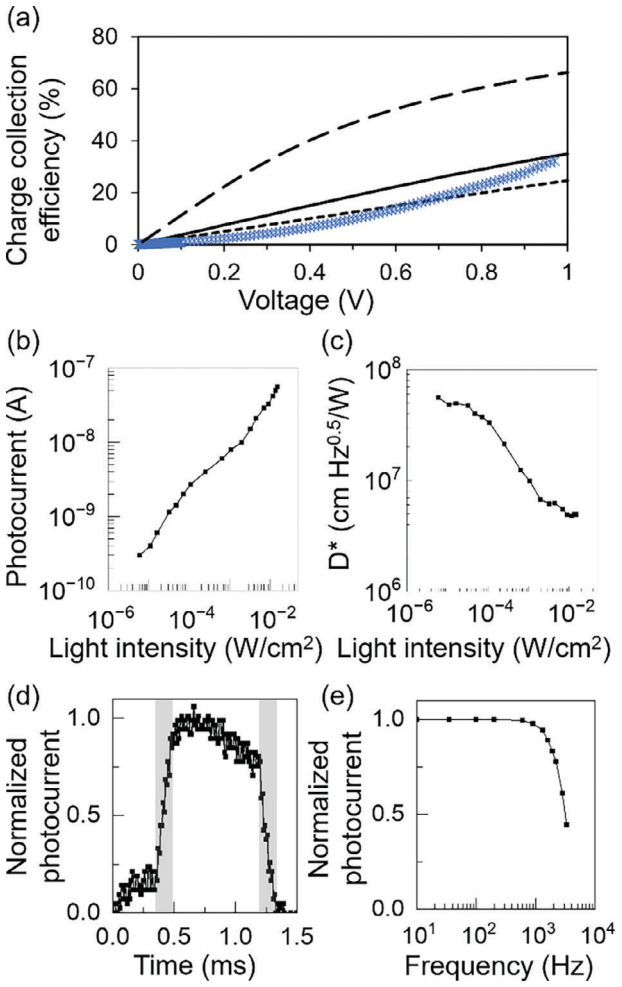

Figure 5. All parts are measured on the photodiode with 1:3 donor:acceptor. The incident light was from a laser diode of 1550 nm wavelength. a) Charge collection efficiency versus applied bias, as a function of $\mu\tau$ values. The blue data was taken on a device under 30 mW cm^{-2} light. The fitting lines are calculated from the Hecht equation based on different $\mu\tau$: 4.5×10^{-10} cm^2 V^{-1} (dashed); 1.5×10^{-10} cm^2 V^{-1} (solid); 1.0×10^{-10} cm^2 V^{-1} (dotted). b) Photocurrent and c) detectivity versus incident light intensity. Parts (b–c) under 0 V bias. Under 16 μW cm^{-2} light, d) Rise and fall times, and e) photoresponse versus incident light frequency, under -0.05 V bias.

efficiency of organic infrared photodiodes from reducing recombination and increasing carrier mobility, such as adjusting molecular structures that increase delocalization[36] and reduce disorder by promoting compact aggregates.

The $\mu\tau$ product is mainly related to limitations in charge collection, but efficiency losses in absorption η_{absorb} and exciton dissociation $\eta_{dissociate}$ also contributed to the low device EQE (EQE = η_{absorb} $\eta_{dissociate}$ $\eta_{collect}$). The charge collection percentage calculated from the Hecht model can be used to compare dissociation and collection efficiencies, to identify how each process affects EQE loss. Given an EQE of ≈0.1% at −0.2 V (Figure 3b) and assuming efficient absorption (η_{absorb} at 80%), with our extracted $\eta_{collect}$ of 8% (Figure 5a), the $\eta_{dissociate}$ was calculated to be 2% [0.001/((0.8)(0.08)) = $\eta_{dissociate}$]. This rough estimation highlights that exciton dissociation efficiency was similarly low as collection efficiency. In order to holistically improve device performance, future work needs to improve the efficiencies of both processes.

2.3. Device Dynamic Range and Temporal Response

When the incident light intensity was adjusted from 5 μW to 10 mW per cm^2, the photocurrent sub-linearly increased from 2 nA to 0.1 μA in Figure 5b. The detectivity lowered with light intensity in Figure 5c, indicative of bimolecular recombination as photogenerated charge population increased. At low light intensity, the detectivity was 4×10^7 $cmHz^{0.5}$ W^{-1}. The temporal response of the photodiode with 1:3 BHJ was measured in Figure 5d, displaying a rise/fall time of 150 μs at −0.05 V. In Figure 5e, the device's −3dB cutoff frequency was found to be 2.4 kHz at -0.05 V, allowing kilohertz response speed.

3. Conclusion

This work evaluated the metrics for organic infrared semiconductors to understand the influence of donor:acceptor ratio on device efficiency, particularly relating the $\mu\tau$ product to explain the better performance of the 1:3 BHJ compared to other composition ratios. The $\mu\tau$ products were validated by complementary measurements and Hecht model fitting. The mobility and recombination time followed opposite trends with the mixture ratios, requiring a balance between minimal disorder for good charge transport and adequate interfacial mixing for extending delocalization and carrier lifetime. The current $\mu\tau$ products in the infrared photodiodes were relatively low, highlighting the need for future work to enhance charge collection by improving aggregate or conjugation designs. Moreover, the collection efficiency calculated from Hecht model can be used to compare whether losses are mainly attributed to dissociation or collection processes, to identify the key bottleneck affecting the overall device efficiency.

4. Experimental Section

Materials Preparation: The donor and acceptor polymers were synthesized as discussed in refs. [1,37], respectively. The chemical solvents were purchased from Sigma and used as received. The donor and the acceptor were dissolved in chlorobenzene at a concentration of 10 mg mL^{-1} and 25 mg mL^{-1}, respectively. The BHJ was a mixture of the donor and acceptor polymers at a weight ratio of 1:1 and 1:3, and it was dissolved in chlorobenzene at a total concentration of 16 and 20 mg mL^{-1}, respectively. For better film formation, 1-chloronaphthalene was added to the BHJ solution to constitute 3% of the total solution volume. The solution was heated at 80 °C and stirred overnight to ensure dissolution of the polymer. The processing and measurements were carried out within a nitrogen glovebox.

ER-EIS Setup: The ER-EIS system was in a three-electrode configuration including a working electrode (WE), a counter electrode (CE), and a reference electrode (RE). The WE was the semiconductor sample on an ITO electrode on top of a glass substrate (sheet resistance of 15Ω/sq, AMG, Korea). A platinum wire (Electron Microscopy Sciences) was used for the CE, and RE is an $Ag/Ag^{[+]}$electrode (CH Instruments). All electrodes were immersed in an electrolyte solution within a well. The electrolyte was 0.1 M $TEABF_4$ in a solvent of propylene carbonate and ethylene carbonate at a 1:1 ratio by volume. The film area exposed to the electrolyte was 0.12 cm^2. The film thicknesses were 250 nm for the neat donor, 150

nm for the neat acceptor, and 200 nm and 180 nm for the 1:1 and 1:3 BHJ, respectively.

The potentiostat was a Bio-Logic SP200. The small sine wave perturbation was 10 mV peak-to-peak in ER-EIS. The sweeping frequency was between 0.1 Hz–1 MHz. To prevent delamination problems due to film swelling from the insertion of electrolyte salt ions,[38,39] the applied voltage scan rates in ER-EIS were fine-tuned to obtain useful data in the shortest possible time.

Device Fabrication: On a glass substrate with patterned ITO electrodes, a 0.07 M precursor solution of tin chloride in ethanol was spin coated at 3000 rpm for 40 s and then annealed at 200 °C for 1 h to form the electron-transporting layer. The semiconductor, which was either the donor, acceptor, or BHJ solution, was spin-coated in two steps where the first step was 800 rpm for 90 s and the second step was 2000 rpm for 5 s, resulting in a film thickness 200 nm for 1D:1A, 180 nm for 1D:3A and 150 nm for acceptor only. Then the hole-transporting materials were deposited by thermal evaporation, with 10 nm molybdenum oxide, and 100 nm of silver electrode to complete the device. The device area was 0.09 cm^2. The device was encapsulated by gluing a glass coverslip onto the substrate, and the devices were measured in the ambient.

Device Characterization: The infrared light source was a 1550 nm laser diode (Thorlabs, part number ML925B45F). The light intensity was controlled by adjusting the driving current to the laser diode controlled by a power supply (Hewlett Packard, HP 6218A) for fixed light intensity. For 3dB test and dynamic range test, a function generator (Rigol, DG 2401A) was used to control the laser diode. A germanium detector from Newport (model: 818IR) was the reference light meter for calibration of the light source intensity. The device current at each applied bias was measured with the electrometer (Keithley 2400). The noise spectral densities were measured using a pre-amplifier (SRS 570) connected to a lock-in amplifier (SRS 530). Temporal signal was acquired using a pre-amplifier connected to an oscilloscope (Rigol, DS1054). The admittance spectroscopy was carried out with the potentiostat Bio-Logic SP200. The small sine wave perturbation was 20 mV peak-to-peak, and the sweeping frequency was between 10 Hz–1 MHz. The sub-bandgap DOS was calculated[25–27] by $DOS(E_\omega) = \frac{-V_{bi}}{qAdk_BT}\frac{\partial C(\omega)}{\partial \ln(\omega)}$, where $E_w = k_BT\ln(\omega_0/\omega)$, where k_B is the Boltzman's constant, T is the temperature, and ω_0 is the rate of trap release and assigned 10^{12} s^{-1} for typical organic photodiodes. $C(\omega)$ is the capacitance at the perturbation frequency ω and V_{bi} is the built-in bias.

Supporting Information

Supporting Information is available from the Wiley Online Library or from the author.

Acknowledgements

B.S. and T.N.N. were supported by the National Science Foundation (NSF) award ECCS-2222203. W.J.K. was supported by the NSF award ECCS-2318990. The work performed at The Georgia Institute of Technology was made possible through the Air Force Office of Scientific Research (AFOSR) under the support provided by the Organic Materials Chemistry Program (Grant FA9550-23-1-0654, Program Manager: Dr. Kenneth Caster) and the NSF award DMR-2323665. This work used the San Diego Nanotechnology Infrastructure of UCSD, which is supported by NSF ECCS-2025752.

Conflict of Interest

The authors declare no conflict of interest.

Data Availability Statement

The data that support the findings of this study are available from the corresponding author upon reasonable request.

Keywords

infrared photodiodes, mobility-lifetime products, organic infrared polymers

Received: October 26, 2024
Revised: December 26, 2024
Published online:

[1] T. Bills, C. T. Liu, J. Lim, N. Eedugurala, P. Mahalingavelar, B. Seo, E. T. Hanna, T. N. Ng, J. D. Azoulay, *Adv. Funct. Mater.* **2024**, *34*, 2314210.
[2] X. Hu, G. Xiao, Y. Li, S. E. Wu, Q. Chen, N. Li, X. Sui, *ACS Appl. Electron. Mater.* **2023**, *5*, 5378.
[3] V. Pecunia, L. Petti, J. Andrews, R. Ollearo, G. H. Gelinck, B. Nasrollahi, J. M. Jailani, N. Li, J. H. Kim, T. N. Ng, H. Feng, Z. Chen, Y. Guo, L. Shen, E. Lhuillier, L. Kuo, V. K. Sangwan, M. C. Hersam, B. Fraboni, L. Basirico, A. Ciavatti, H. Wu, G. Niu, J. Tang, G. Yang, D. Kim, D. Dremann, O. Jurchescu, D. Bederak, A. Shugla, et al., *Nano Futures* **2024**, *8*, 032001.
[4] C. Wang, X. Zhang, W. Hu, *Chem. Soc. Rev.* **2020**, *49*, 653.
[5] H. M. Luong, S. Chae, A. Yi, K. Ding, J. Huang, B. M. Kim, C. Welton, J. Chen, H. Wakidi, Z. Du, H. J. Kim, H. Ade, G. N. M. Reddy, T. Q. Nguyen, *ACS Energy Lett.* **2023**, *8*, 2130.
[6] P. Jacoutot, A. D. Scaccabarozzi, D. Nodari, J. Panidi, Z. Qiao, A. Schiza, A. D. Nega, A. Dimitrakopoulou-Strauss, V. G. Gregoriou, M. Heeney, C. L. Chochos, A. A. Bakulin, N. Gasparini, *Sci. Adv.* **2023**, *9*, eadh2694.
[7] T. Li, G. Hu, L. Tao, J. Jiang, J. Xin, Y. Li, W. Ma, L. Shen, Y. Fang, Y. Lin, *Sci. Adv.* **2023**, *9*, eadf6152.
[8] I. Park, C. Kim, R. Kim, N. Li, J. Lee, O. K. Kwon, B. Choi, T. N. Ng, D.-S. Leem, *Adv. Opt. Mater.* **2022**, *10*, 2200747.
[9] D. B. Sulas, A. E. London, L. Huang, L. Xu, Z. Wu, T. N. Ng, B. M. Wong, C. W. Schlenker, J. D. Azoulay, M. Y. Sfeir, *Adv. Opt. Mater.* **2018**, *6*, 1701138.
[10] J. H. Vella, L. Huang, N. Eedugurala, K. Mayer, T. N. Ng, J. Azoulay, *Sci. Adv.* **2021**, *7*, abg2418.
[11] C. T. Liu, J. Vella, N. Eedugurala, P. Mahalingavelar, T. Bills, B. Salcido-Santacruz, M. Y. Sfeir, J. D. Azoulay, *Adv. Sci.* **2023**, *10*, 2304077.
[12] J. Benduhn, K. Tvingstedt, F. Piersimoni, S. Ullbrich, Y. Fan, M. Tropiano, K. A. McGarry, O. Zeika, M. K. Riede, C. J. Douglas, S. Barlow, S. R. Marder, D. Neher, D. Spoltore, K. Vandewal, *Nat Energy* **2017**, *2*, 17053.
[13] R. A. Street, A. Krakaris, S. R. Cowan, *Adv. Funct. Mater.* **2012**, *22*, 4608.
[14] R. A. Street, M. Schoendorf, A. Roy, J. H. Lee, *Phys. Rev. B* **2010**, *81*, 205307.
[15] O. J. Sandberg, C. Kaiser, S. Zeiske, N. Zarrabi, S. Gielen, W. Maes, K. Vandewal, P. Meredith, A. Armin, *Nat. Photonics* **2023**, *17*, 368.
[16] S. Gielen, C. Kaiser, F. Verstraeten, J. Kublitski, J. Benduhn, D. Spoltore, P. Verstappen, W. Maes, P. Meredith, A. Armin, K. Vandewal, *Adv. Mater.* **2020**, *17*, 2003818.
[17] R. Wu, Y. Kang, D. Fan, P. Li, Y. Li, D. Wei, S. Wu, T. Tan, G. Zha, *IEEE Trans. Nucl. Sci.* **2024**, *71*, 352.
[18] T. N. Ng, W. S. Wong, R. A. Lujan, R. A. Street, *Adv. Mater.* **2009**, *21*, 1855.
[19] L. G. Gerling, S. Mahato, S. Galindo, C. Voz, J. Puigdollers, R. Alcubilla, J. M. Asensi, in *10th Spanish Conf. on Electron Devices*, **2015**.
[20] G. Dennler, A. J. Mozer, G. Juška, A. Pivrikas, R. Österbacka, A. Fuchsbauer, N. S. Sariciftci, *Org. Electron.* **2006**, *7*, 229.
[21] T. Kirchartz, T. Agostinelli, M. Campoy-Quiles, W. Gong, J. Nelson, *J. Phys. Chem. Lett.* **2012**, *3*, 3470.

[22] M. Stolterfoht, A. Armin, B. Philippa, R. D. White, P. L. Burn, P. Meredith, G. Juška, A. Pivrikas, *Sci. Rep.* **2015**, *5*, 9949.
[23] H. Bässler, D. Kroh, F. Schauer, V. Nádaždy, A. Köhler, *Adv. Funct. Mater.* **2021**, *31*, 2007738.
[24] F. Schauer, V. Nádazdy, K. Gmucová, *J. Appl. Phys.* **2018**, *123*, 161590.
[25] R. A. Street, Y. Yang, B. C. Thompson, I. McCulloch, *J. Phys. Chem. C* **2016**, *120*, 22169.
[26] W. Yao, Z. Wu, E. Huang, L. Huang, A. E. London, Z. Liu, J. D. Azoulay, T. N. Ng, *ACS Appl. Electron. Mater.* **2019**, *1*, 660.
[27] N. Li, I. Park, J. H. Vella, S. J. Oh, J. D. Azoulay, D.-S. Leem, T. N. Ng, *ACS Appl. Mater. Interfaces* **2022**, *14*, 53111.
[28] S. E. Wu, L. Zeng, Y. Zhai, C. Shin, N. Eedugurala, J. D. Azoulay, T. N. Ng, *Adv. Sci.* **2023**, *10*, 2304688.
[29] B. Seo, J. Chung, N. Eedugurala, J. D. Azoulay, H. J. Kim, T. N. Ng, *ACS Appl. Electron. Mater.* **2023**, *5*, 6401.
[30] S. Athanasopoulos, F. Schauer, V. Nádaždy, M. Weiß, F. J. Kahle, U. Scherf, H. Bässler, A. Köhler, *Adv. Energy Mater.* **2019**, *9*, 1900814.
[31] F. Schauer, V. Nádady, K. Gmucová, T. Váry, *J. Appl. Phys.* **2018**, *124*, 165702.
[32] S. Alam, V. Nádaždy, T. Váry, C. Friebe, R. Meitzner, J. Ahner, A. Anand, S. Karuthedath, C. S. P. De Castro, C. Göhler, S. Dietz, J. Cann, C. Kästner, A. Konkin, W. Beenken, A. M. Anton, C. Ulbricht, A. Sperlich, M. D. Hager, U. Ritter, F. Kremer, O. Brüggemann, U. S. Schubert, D. A. M. Egbe, G. C. Welch, V. Dyakonov, C. Deibel, F. Laquai, H. Hoppe, *J. Mater. Chem. C* **2021**, *9*, 14463.
[33] D. Kroh, S. Athanasopoulos, V. Nádaždy, F. J. Kahle, H. Bässler, A. Köhler, *Adv. Funct. Mater.* **2024**, *34*, 2302520.
[34] T. N. Ng, B. Russo, A. C. Arias, *J. Appl. Phys.* **2009**, *106*, 094504.
[35] P. N. Murgatroyd, *J. Phys. D: Appl. Phys.* **1970**, *3*, 151.
[36] Y. C. Wei, S. F. Wang, Y. Hu, L. S. Liao, D. G. Chen, K. H. Chang, C. W. Wang, S. H. Liu, W. H. Chan, J. L. Liao, W. Y. Hung, T. H. Wang, P. T. Chen, H. F. Hsu, Y. Chi, P. T. Chou, *Nat. Photonics* **2020**, *14*, 570.
[37] K. Wang, L. Huang, N. Eedugurala, S. Zhang, M. A. Sabuj, N. Rai, X. Gu, J. D. Azoulay, T. N. Ng, *Adv. Energy Mater.* **2019**, *9*, 1902806.
[38] K. Kwon, T. N. Ng, *Org. Electron.* **2014**, *15*, 294.
[39] S. Ready, F. Endicott, G. Whiting, T. N. Ng, E. Chow, J.-P. Lu, *NIP & Digital Fabrication Conference* **2013**, *29*, 9.